ADVANCED RAMAN SPECTROSCOPIES FOR LIFE SCIENCES APPLICATIONS

ANTONIO SASSO, GIUSEPPE PESCE, GIULIA RUSCIANO, GIANLUIGI ZITO
Department of Physics "E. Pancini", University of Naples Federico II, Naples, Italy

Raman effect is an old-dated phenomenon that was discovered in 1921 by the Indian physicist C.V. Raman. Since then, Raman Spectroscopy (RS) has found a plethora of applications, especially in life sciences, thanks to its intrinsic chemical identification capability based on vibrational spectroscopy and noninvasiveness due to light probing. Recently, RS is experiencing a further renewed interest. Novel nano-photonic techniques aimed at controlling electromagnetic phenomena at length scales much shorter than the wavelength of light have been integrated with the Raman process, pushing the limit of the technique at the frontiers of science. The interaction between optical fields and metal nanostructures gives place to localized surface plasmon resonances. Surface Enhanced Raman Scattering (SERS) is the variant of spontaneous RS that makes use of this effect. Interestingly, SERS allows exceeding RS detection limits reaching sensitivities up to the level of single-molecule detection. Moreover, the ability to trigger plasmon resonances on the apical part of structured tips used in scanning probe microscopy has also made possible to realize optical nano-antennas capable of shining surfaces at the nanoscale, hence enabling a simultaneous morphological and biochemical analysis of bio-systems. This is the principle of Tip Enhanced Raman Scattering (TERS). In this article, an overview of conventional and advanced Raman techniques is given. The basic physical principles of Raman spectroscopy and its variants (SERS and TERS) are briefly discussed. Finally, a few but representative examples of applications for cell membrane analysis are presented.

Shikuan Yang, Birgitt Boschitsch, and Tak-Sing Wong, The Pennsylvania State University

1 Introduction

The interaction between light and matter has been crucial for the knowledge we have today about the nature of atoms and molecules: it was the pioneering work of spectroscopists, in fact, to lay the foundation for the birth of quantum mechanics.

The effective use of the light does not seem to be exhausted. Optical methods are still proving to be ideal tools for exploring, with minimal invasiveness and with spatial resolution below the limit of the diffraction of light, the complexity of biological systems. Today, Bio-photonics denotes an area of research that deals with the use of photonic techniques applied to the study of biological systems [1]. Its mission is to understand the inner functionality of individual microorganisms (cells, bacteria and viruses), or even individual bio-macromolecules. These interdisciplinary approaches have recently made possible to highlight the peculiar function of individual proteins, DNA strands and other important molecules. In medicine, the advent of bio-photonics has introduced new methods to achieve the imaging potential of living cells, very promising for early diagnosis of diseases and their treatments.

Laser-based fluorescence microscopy has been traditionally considered as the golden standard for optical bio-imaging due to its high sensitivity and facile preparation of samples (staining). Generally, fluorescence imaging is achieved by using fluorophores that selectively bind to target molecules.

Their high quantum yields allow to achieve single-molecule sensitivity; that allows, for instance, to track proteins motion across different cell regions (membrane, cytoplasm, nucleus, etc). Although the new super-resolution fluorescence microscopy techniques, as stimulated emission depletion (STED) microscopy [2], are used for bio-imaging at the impressive resolution of a few tens of nanometres, fluorescent labels suffer of some significant limitations due to: i) photobleaching and photoblinking of the fluorophores; ii) perturbation of the investigated molecules caused by the anchoring of the fluorophores themselves; and iii) poor chemical selectivity. Raman Spectroscopy (RS), instead, seems to overcome all these limitations because: i) it is quenching-free since based on light scattering, not absorption; ii) it does not require any sample preparation (label-free); iii) and, still more important, it assesses the chemical composition of the sample by exploiting the vibrational structure of molecular bonds, which is the basis of the so-called chemical finger-printing. These advantages have led to a remarkable development of RS-based techniques making them rise as powerful analytical methods, not only in physics and chemistry but in many other interdisciplinary fields like cultural heritage [3], food [4], forensic sciences [5], biology [6] and life sciences [7].

However, also RS has several limitations, the most severe of them is the quite low efficiency of inelastic light scattering. This drawback can be overcome by several alternative techniques, including Resonant Raman Spectroscopy (RRS) [8], Coherent Anti-Stokes Raman Spectroscopy (CARS) [9] or Stimulated Raman Spectroscopy (SRS) [10].

Another alternative method to enhance the weak Raman signal is the basis of Surface-Enhanced Raman Scattering (SERS) [11]. Localized surface plasmon resonances (LSPRs) at the boundaries of metal-dielectric nanostructures, that are collective resonant oscillations of conduction electrons, may provide an amplification of the electromagnetic field, in the near-field, up to 3 orders of magnitude. The amplification of the electromagnetic field is associated to the squeezing of the excitation electromagnetic field to volumes comparable with molecular sizes into the so-called hot spots. When molecules are adsorbed to noble-metal nanostructures whose geometry is resonant with excitation light, they are "illuminated" by such an intense evanescent optical field so that Raman light scattered in the far field is amplified up to a factor $(10^3)^4 = 10^{12}$ because the process involves the intensity of the amplified excitation field and amplified Raman field, both at frequencies within the range of the relatively broad plasmonic resonance of the metal-dielectric nanostructure (the dielectric component is mainly air or water). Therefore, this mechanism leads to a high sensitivity of chemical compounds, offering the capability of detecting single molecules [12]. However, spatial resolution of SERS is diffraction-limited because SERS is a far-field technique. The spatial resolution limit can be removed by combining the chemical sensitivity of SERS with the high spatial resolution of scanning probe microscopies, like Atomic Force Microscopy (AFM). The new technique, called Tip Enhanced Raman Scattering (TERS) [13], enables simultaneous chemical and morphological imaging of surfaces at the nanometre length-scale thanks to scanning probes having a nanometre scale structure. This technique is realized by illuminating a metallic (or metaled) tip with radius of curvature down to 10 nm by a tightly focused laser beam. Plasmon resonance can be hence localized at the tip apex, or between the tip and a bottom plasmonic surface. As a consequence, the tip acts as a sort of nano-antenna able to provide a strong amplification of the Raman signal of the molecules adsorbed to the surface offering a spatial resolution not limited by diffraction [14, 15].

This review is divided into two parts. The first part sets out the general principles of RS and its variants, as SERS and TERS. The second part is devoted to some applications to biological systems.

2 Spontaneous and amplified Raman Spectroscopies

2.1 Spontaneous Raman Spectroscopy

What is now called Raman Scattering is an effect discovered by Sir C. V. Raman in 1921 in India. Raman observed the frequency shift of scattered light from liquid samples and called it as "modified scattering" to distinguish it from (elastic) Rayleigh scattering. This discovery led him to be awarded the Nobel prize for physics in 1930. In his explanation of the new phenomenon, Raman showed that the frequency shift depended on the investigated molecule and was independent of the frequency of the incident light. Interestingly, despite the weakness of the signals, Raman observed the effect by quite rudimentary devices, using the Sun as a light source and a violet filter to isolate a band of violet light incident on a liquid sample and a second green glass to select the shifted scattered light. Finally, he used his own dark-adapted eyes as detectors, proving so the capability of the human eye to detect extremely low level of photon flux (even single photon) over a high dynamic range.

In the photon picture, the scattering of light can be seen as elastic or inelastic collisions between photons and molecules (see fig. 1). From the
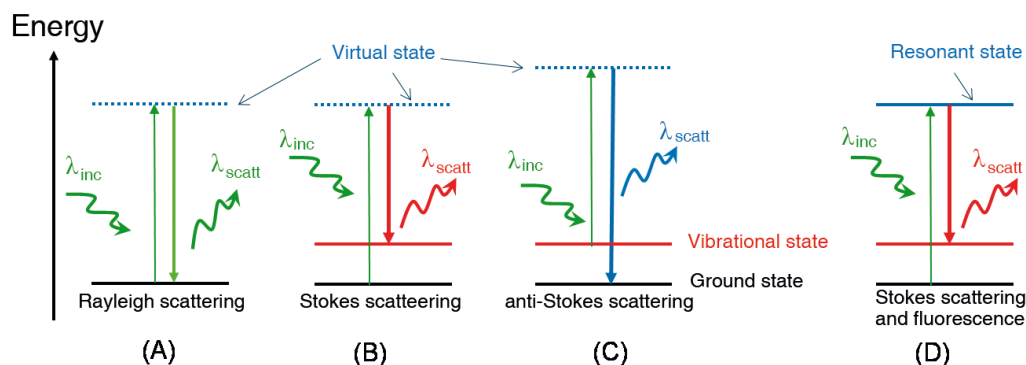
Fig. 1 Energy level diagram for Rayleigh (A), Stokes (B), and anti-Stokes (C) Raman scattering. When the excited level coincides with a real state the Raman scattering is accompanied by fluorescence (D).

virtual state, molecules may decay following three different paths. Most of them return back to the initial state through the emission of a photon having the same energy of the incident photon (see fig. 1 A).

This elastic process, named Rayleigh scattering, is for instance responsible of the blue colour of the sky caused by the scattering of sunlight in the atmosphere. Inelastic scattering is originated when molecules decay toward an excited vibrational level (see fig. 1 B), or when molecules lying in an initial vibrational state decay toward the ground state (see fig. 1 C). These two processes are called Stokes and anti-Stokes scattering, respectively; the energy difference of the scattered photon is released to the molecule (Stokes photons) or subtracted from it (anti-Stokes photons).

Since different molecules have bonds vibrating at well-defined frequencies/energies, it turns out that the Raman spectrum consists of quite sharp peaks representing the actual "chemical fingerprint" of the molecule.

The intensity of the Raman signal I_{Raman} depends on

$$(1) \qquad I_{Raman} \propto N \cdot I_0 \left(\frac{\partial \alpha}{\partial r} \right)^2 \cdot \sigma \,,$$

being N the number of molecules involved in the scattering and I_0 the laser intensity. The term $\partial \alpha / \partial r$ denotes that only vibrations changing polarizability α yield Raman scattering.

The Raman cross section σ, which indicates the probability with which scattering occurs, depends on the specific molecular vibration and it decreases with the fourth power of the incident wavelength ($\sigma \propto \lambda^{-4}$). Hence, ultraviolet (UV) radiation would be more advantageous but this contrasts with biological applications because the UV light more easily induces photodamages, effects that are greatly reduced moving to the near-infrared (IR) region.

As order of magnitude $\sigma = 10^{-30} - 10^{-25}$ cm^2/sr for visible light, *i.e.* about ten orders of magnitude weaker than fluorescence. Stokes signals are in turn ~10^6 times weaker than Rayleigh signals while anti-Stokes signals are still weaker by a factor ~ 10^3 than Stokes ones due to the Boltzmann statistics ($N \propto e^{-\Delta E / kT}$).

For short wavelengths (blue-UV), the incident photon could be resonant with electronic states of the molecule (fig. 1 D); in this case the Raman cross section becomes comparable with the absorption or fluorescent cross section, but fluorescence occurs simultaneously, which can mask the weaker Raman signals.

In principle, the Raman spectrum provides similar information as the IR absorption spectrum, but, since the two phenomena are regulated by different physical mechanisms, a vibrational mode may be either IR active or Raman active, but not both, *i.e.* the relative selection rules are in some way complementary. As a rule of thumb, symmetric vibrational modes are Raman active while asymmetric ones are IR active. Interestingly, water exhibits a high IR activity but a low Raman activity. Since water represents the main constituent of biological systems, this is another advantage of using RS for studying bio-systems.

In addition, when RS is combined with confocal optical microscopy (micro-RS) the probe volume decreases to few femtolitres (with light spot diameter below 1 mm). With this resolution, it is possible to acquire Raman spectra on two- or three-dimensional arrays of points, reconstruct the Raman imaging of the sample selecting a particular band of the biochemical component of interest, which is the basis of hyperspectral mapping.

From an experimental point of view, RS is realized by focusing onto the sample a laser beam with a high-numerical-aperture objective lens. Scattered photons are usually collected with the same objective; by rejecting the intense elastic scattered light by a notch filter and dispersing the scattered photons with a diffraction grating, the inelastic Raman spectrum is finally detected by means of sensitive CCD cameras (see fig. 2).
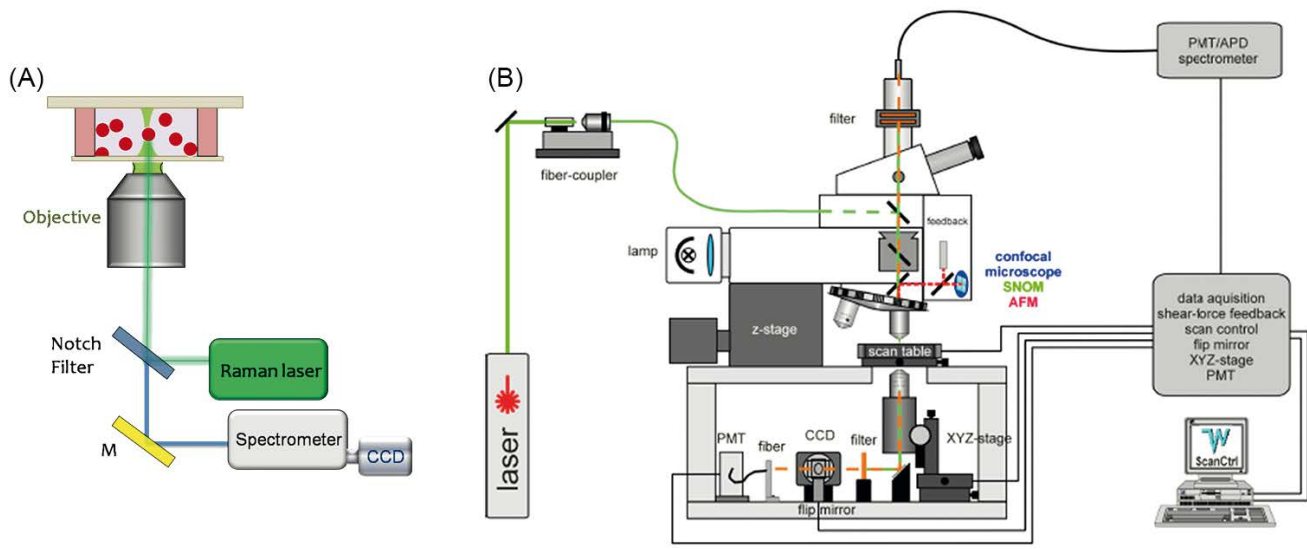
Fig. 2 (A) Essential of a typical micro-Raman set-up. Photons emitted from a visible laser source are focused on the sample by an objective lens. Scattered photons are collected with the same objective and, those transmitted by a notch filter, are sent to a spectrometer equipped with a CCD-camera. (B) Schematic layout of our confocal micro-Raman setup WiTec alpha 300 (`http://witec.de`) consisting of two microscopes (one inverted, from the lower side, and one directed, from the upper side) combined with an atomic force microscope for TERS and scattering-type near-field optical microscopy (SNOM).

2.2 Surface Enhanced Raman Scattering

Historically, SERS birth dates back to 1974 when Fleishmann and co-workers [16] observed an anomalous enhancement of the Raman signal from pyridine molecules adsorbed over a roughened silver surface. Few years later, the physical interpretation of the phenomenon based on the excitation of localized surface plasmon resonances was provided [17, 18]. Nevertheless, even 40 years after its discovery, a full understanding of the mechanisms behind this phenomenon is still debated. Very recently, a new general interpretation of the origin of field enhancement has emerged [19].

A simple model to describe LSPRs assumes a small metal sphere illuminated by light in which the time-varying electromagnetic (EM) field of the illuminating light excites collective oscillating surface plasmon multipoles. In contrast to propagating surface plasmon polaritons, when the size of the metallic structure is small compared to the wavelength of the incident radiation, the plasmon is confined to the local nanostructure with no propagation along the surface and gives rise to a localized surface plasmon resonance. The LSPR can be viewed as a peak in the extinction spectrum of the nanoparticle (NP). It is not difficult to image that the LSPR depends critically not only on the NP size and shape but also on the dispersion of the metal (dielectric function) and surrounding material. This scattering property has attracted considerable interest since ancient times when metallic NPs (unconsciously) were used as decorative pigments in stained glasses and artworks. The most famous example of such applications is the Lycurgus Cup, a 4th-century Roman glass cage cup, which exhibits a different colour depending on whether or not light is passing through it. Within the electrostatic approximation (*i.e.* optical electric field is assumed constant over particle size) an analytical solution of Maxwell equations exists for simple geometries as a sphere (Mie theory). In this case, it is possible to demonstrate that the polarizability of the induced dipole is given by

$$(2) \qquad \alpha = V \frac{\varepsilon - \varepsilon_m}{\varepsilon + 2\varepsilon_m},$$

where V is the particle volume, $\varepsilon = \varepsilon_r + i\varepsilon_{im}$ is the complex frequency-dependent dielectric function of the metal, and ε_m is the dielectric function of the surrounding medium.

As a matter of fact, a molecule in proximity to the sphere at distance d from the NP surface is exposed to a
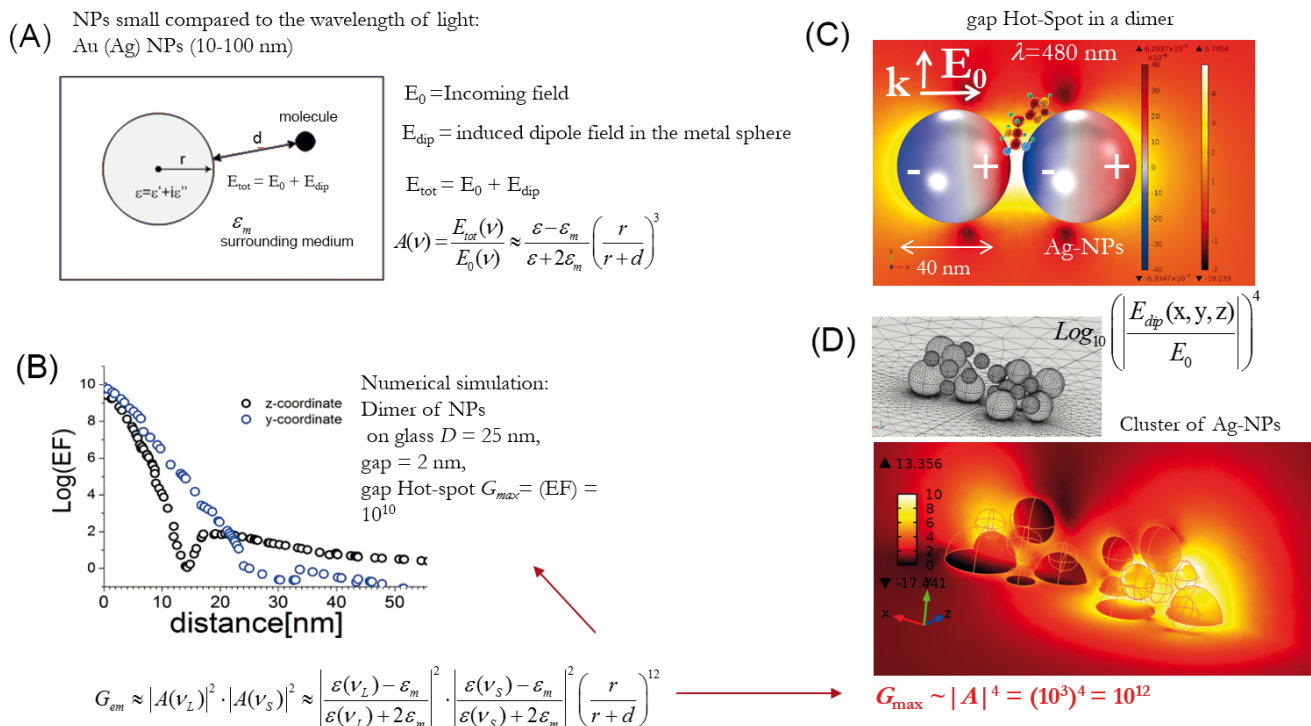
Fig. 3 Simple description of SERS: (A) a metal nanoparticle illuminated by light gives place to oscillation of the free electrons of the surface that in (C) are depicted as surface charge modes (calculated with a numerical solver). In (A), a molecule is placed at nanometric distance d from the NP surface and is affected by an amplified optical field. (B) Amplification dependence on the distance from the hot spot located at the centre of a dimer of NPs. (C) EF map with overlaid surface charge modes over the surface of a dimer of NPs: the amplification is large in the gap hot spot where a molecule is representatively depicted. In (D), the extraordinary large EF (10^{12}) that is achievable on complex nanostructures like aggregates of NPs with nanometre gaps at resonant excitation.

near field E_{tot} which is the superposition of the incoming field E_0 and the field of the dipole E_{dip} induced in the metal nanosphere. This field assumes the form

$$(3) \qquad E_{tot} = E_0 + E_{dip} = E_0 + r^3 \frac{\varepsilon - \varepsilon_m}{\varepsilon + 2\varepsilon_m} E_0 \frac{1}{(r + d)^3} \ .$$

It is possible to define an enhancement gain as the ratio of the total field E_{tot} at the molecule position and the incoming field E_0:

$$(4) \qquad A(\nu_L) = \frac{E_{tot}}{E_0} \sim \frac{\varepsilon - \varepsilon_m}{\varepsilon + 2\varepsilon_m} \left(\frac{r}{r + d} \right)^3 .$$

The most important feature of this equation is the presence of the denominator $\varepsilon + 2\varepsilon_m$. Assuming the imaginary part of the dielectric function to be negligible ($\varepsilon_{im} \sim 0$, typical for silver in the visible and IR spectrum and for gold above 600 nm), a strong resonance occurs at the laser frequency ν_L for which $\varepsilon = -2\varepsilon_m$. In an analogous fashion, the Stokes field of the molecule dipole is enhanced too, and if its frequency is close to the LSP resonance, the global intensity enhancement factor can be written as

$$(5) \qquad G_{em} = |A(\nu_L)|^2 |A(\nu_S)|^2 \sim \left| \frac{\varepsilon(\nu_L) - \varepsilon_m}{\varepsilon(\nu_L) + 2\varepsilon_m} \right|^2 \left| \frac{\varepsilon(\nu_S) - \varepsilon_m}{\varepsilon(\nu_S) + 2\varepsilon_m} \right|^2 \left(\frac{r}{r + d} \right)^{12} .$$

Equation (5) shows that the SERS gain scales as the forth power of the local field and drops off rapidly with distance from the surface, as $1/d^{12}$, which is responsible for the local character of SERS enhancement (ranging from 0 to ~20 nm) (fig. 3 A, B).

To compare the response of spontaneous (I_{Raman}) and SERS (I_{SERS}) signals, the Enhancement

Factor (EF) is introduced. It is defined as the ratio between SERS and spontaneous Raman signals, properly normalized to the number of molecules (N_{SERS} and N_{Raman}) involved in the respective processes:

$$(6) \qquad EF = \frac{I_{SERS}}{I_{Raman}} \frac{N_{Raman}}{N_{SERS}}.$$

For noble metals (gold, silver, and copper) the resonance condition can be satisfied at visible frequencies and for nanoparticles (NPs) with size in the range 10–100 nm. An additional level of complexity of the plasmon resonances, but also of great interest, arises from the existence of coupled plasmon resonances for two or more closely spaced objects. Considering, for instance, the very simple case of two metallic nanospheres (fig. 3 C), it is possible to demonstrate that resonance coupling produces a red shift of the plasmon resonance, with a further enhancement of the intensity concentrated in the middle of the two spheres, as shown in fig. 3 C. The positions where maximum SERS amplification occurs were called for the first time "hot spots" by Martin Moskovits [20].

Metal NPs absorption and scattering properties can be tuned by controlling the light polarization, particle size, shape, and the local refractive index near the particle surface. As a general rule, as the size increases, the NPs resonances i) shift to the red, ii) are strongly damped and spectrally broadened, and iii) other resonances appear, which are typically related to the activation of multipolar resonances (quadrupolar resonances etc.).

The enhancement effect so far described is commonly referred to as "electromagnetic enhancement". However, since SERS effect can also show a molecular selectivity, this suggests the existence of an additional SERS enhancement mechanism of chemical origin. Among the different mechanisms proposed to explain this chemical effect, the charge transfer mechanism seems to be the most reliable. In particular, it is described as a four-steps process, involving the transfer of a charge from the metallic nanostructure to the molecule and back. However, the chemical SERS enhancement mechanisms contribute to the enhancement only by a factor of $10 - 10^3$.

Although, in the last decades, a great effort has been dedicated to the synthesis and fabrication of high-performance SERS substrates in terms of sensitivity and reproducibility, this topic is still open because reproducibility of SERS detection is mined by the strong localization of the hot spots [21]. There is a large body of existing methods for the synthesis of nanoparticles (NPs), the fundamental basis of SERS substrates. Traditionally, the most widespread ones are solution-phase synthesis techniques (*i.e.* related to the family of bottom-up techniques), one of which is Lee-Meisel

method [22]. However, colloidal SERS substrates suffer from insufficient spatial reproducibility due to their intrinsic local geometric heterogeneity which induces an uncontrollable position-dependent enhancement. On the contrary, top-down methods, dealing with electron/ion beam lithography techniques actually produce highly ordered NPs with a narrow shape and size distribution on substrates, but such techniques are quite time-consuming, require expensive equipment, and spatial resolution is typically above 10–20 nm.

In our laboratory, we have recently developed an alternative method based on a chemical procedure which gives very regular NPs structures with high efficiency and SERS spatial reproducibility. The method makes use of block copolymer (BCP) micelles of polystyrene-block-poly-4-vinylpyridine (PS-b-P4VP) loaded with silver nanoparticles (Ag-NPs). Details on the fabrication procedure is described in ref. [23] and schematically depicted in fig. 4 A. Briefly, thin films of self-assembled templates of silver NPs are produced by fast solvent evaporation via spin-coating over glass coverslips, then polymers are removed upon UV exposure.

At the end of our procedure, a typical nearly hexagonal lattice consisting of an Ag-NPs cluster is hence obtained (fig. 4 B). The average nanoisland diameter $D \sim 30$ nm and the separation gap $g < 10$ nm. Each nano-island consists in turn of closely spaced NPs of size in the range ~ 1–12 nm (fig. 4 B, inset). In order to increase the nanoislands packing density we further modified the standard procedure [24] by processing a higher concentrated Ag-BCP solution with centrifugation, filtration and slow spin-coating treatment as described in ref. [23]. In such way we obtained a self-assembled isotropic nanostructure with characteristics of homogeneity typical of the so-called disordered hyperuniform pattern [25, 26]. Such kind of nanostructure is characterized by a novel long-range correlated disordered configuration in which fluctuations of the number variance increase linearly with the probed area radius, whereas for a two-dimensional random point-process system a quadratic dependence is expected [27] (fig. 5). As final result we produced a distortion of the hexagonal lattice reducing the gap to ~ 2 nm. The increased cluster density, and the resulting correlated-random nanoisland pattern gave higher quality SERS performances, starting from the hot-spot density which resulted $\sim 10^4 /\mu m^2$. Under such circumstances, we observed a suppression of one order of magnitude in the SERS signal fluctuations with an average relative standard deviation $\sigma /\langle EF \rangle$ of 3.6% over cell-scale regions (2500 mm^2) [23]. Typical EF values found for our substrate were enough to detect single molecules of Raman resonant dyes.

Starting from BCP self-assembling technology, we have recently demonstrated the possibility to functionalize AFM
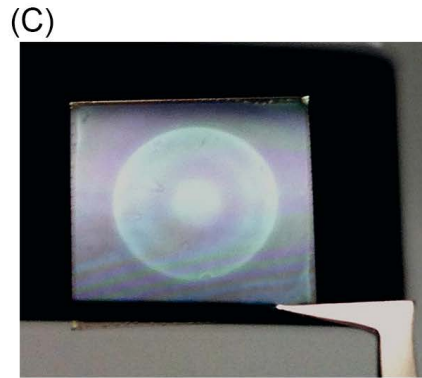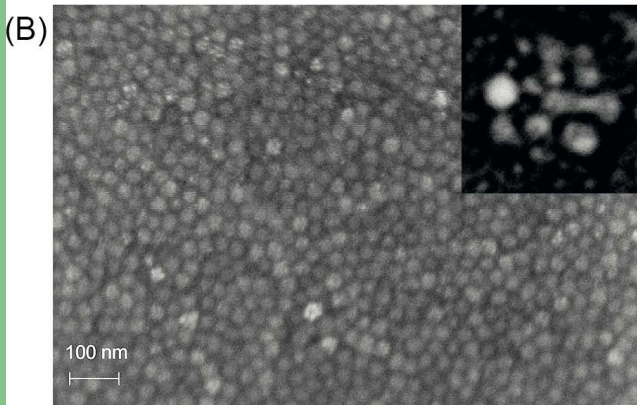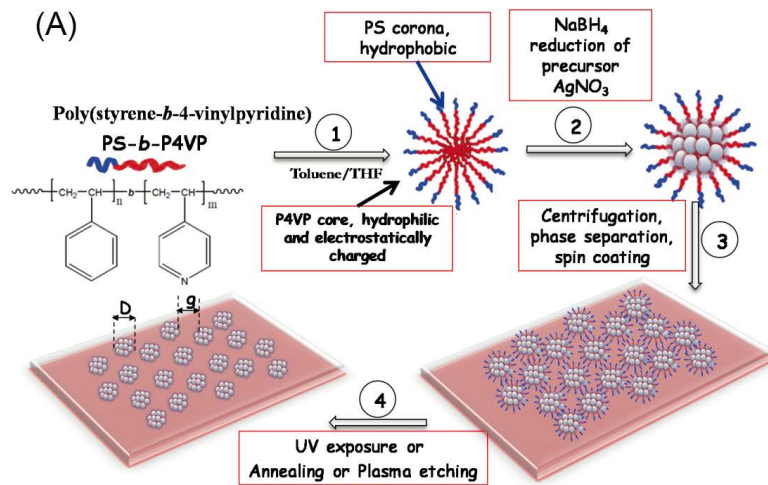
Fig. 4 (A) The various stages of the procedure for SERS substrate fabrication. 1) Block-copolymers (polystyrene-block-poly-4-vinylpyridine – PS-b-P4VP) are diluted in toluene/THF in which they form micelles; 2) micelles are loaded with $AgNO_3$, then reduced to metal by $NaBH_4$; 3) thin films of nearly-hcp self-assembled loaded micelles are produced by fast solvent evaporation via spin-coating over glass coverslips; 4) polymers are removed with UV exposure. (B) Scanning electron micrograph of the nanostructure. The inset shows a transmission electron micrograph of a single cluster of nearly 30 nm of diameter. (C) Photograph of the large-area sample (side 24 mm) showing a strong green backscattering (in transmission the film appears reddish).
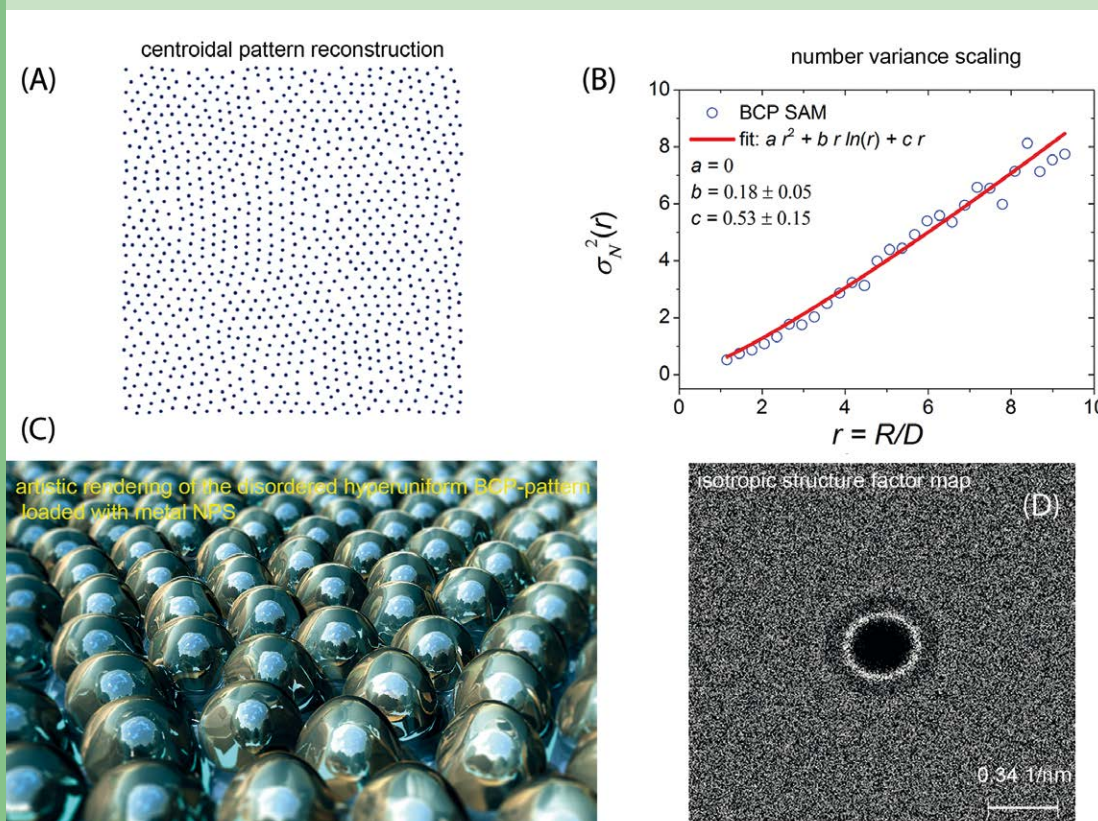

Fig. 5 (A) Controidal pattern reconstructed from an AFM micrograph of the final random pattern obtained by applying our protocol: the filling fraction is highly increased inducing nanoisland gaps of 2–3 nm. (B) Linear scaling of the number variance σ_N^2 as a function of the sampling window normalized radius R/D. (C) Artistic rendering of the metal-loaded BCP pattern. (D) Characteristic ring-shaped structure factor $S(q)$ of the random nanostructure shows radial isotropy and suppression of long-range fluctuations evidenced by $S(q \rightarrow 0) \simeq 0$.
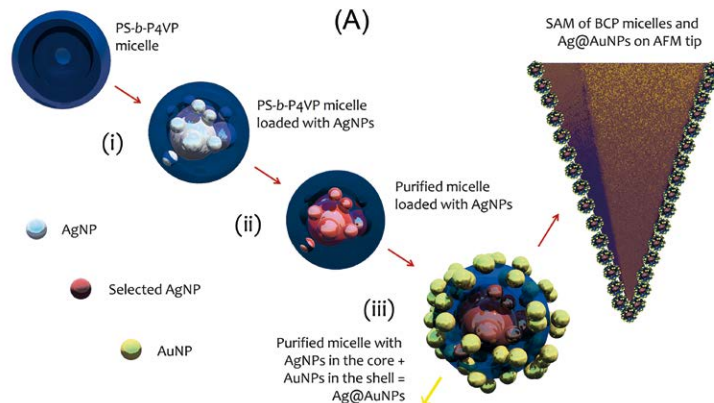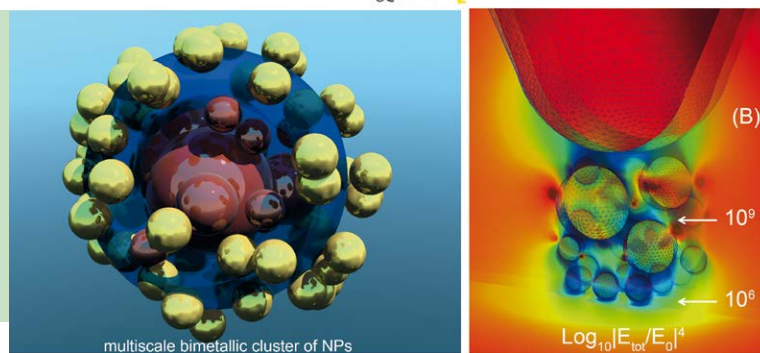
Fig. 6 (A) Schematics of the chemical synthesis and deposition of metal-loaded BCP pattern on AFM scanning probes. (B) Map of the EF around an apical cluster of NPs on a silicon tip apex.

scanning probes for TERS applications [28]. In fig. 6 A, a schematic layout of the chemical procedure is depicted, which finally allows to achieve a bimetallic structure in the BCP-micelle with silver (Ag) and gold (Au) NPs, transferred by virtue of dip-coating on an AFM probe tip. This allows one to tune the plasmonic response of the tip. At same time, the cluster provides a strong near-field enhancement as calculated in fig. 6 B, capable of challenging TERS scanning on thick biological samples like bacterial spores. The electromagnetic enhancement of NPs architectures for SERS can be simulated by means of 3D numerical finite-element methods which allow one to solve numerically Maxwell's equations with appropriate boundary conditions. Simulations are very precious to design and to optimize plasmonic architectures exploring the role of many physical parameters, as already shown in fig. 3 C, D. In fig. 6 B, the spatial distribution of the EF is approximated as the fourth power of the norm E of the scattered electric field normalized to the incident radially polarized wave field, of amplitude E_0 at $\lambda = 520$ nm (bottom illumination); surrounding medium index $n = 1.4$. The tomographic representation of the field amplification is rendered by means of 3 overlaid transparent cut planes at $z = -7, 0, 8$ nm and a y-planar cut 0.5 nm below Au-NPs. The enhancement factor is saturated at 10^6: regions of such level fill and surround the apical cluster. The chain coupling from the center to the peripherical NPs transmits

local field amplification to the surface of Au-NPs. Details can be found in ref. [28].

2.3 Tip-Enhanced Raman Scattering

As mentioned above, the intrinsic random distribution of SERS substrates, even those which show an apparent very regular structure, makes the position of the hot spots random. This unpredictable localization undermines the potential sub-diffraction character of SERS which remains limited by the diffraction of light. The TERS technique overcomes this limit because the plasmon resonance is spatially localized at the apex of a Scanning Probe Microscopy (SPM) tip. The direct advantage is an impressive improvement of resolution but the disadvantage is the reduction in the intensity of the SERS signal due to the reduced number of the molecules in the vicinity of the tip. More generally, TERS is one of several types of optical techniques based on the confinement of the light at nanometer length scales (nano-optics) [29], developed to overcome the diffraction limit of light microscopy. It was theoretically predicted in 1985 [30] and experimentally realized in 2000 [31]. Unlike scanning and transmission electron microscopies (SEM, TEM), that require often sample preparation and operating working conditions of high vacuum, TERS analyses samples as they are either in air or in aqueous media [32].

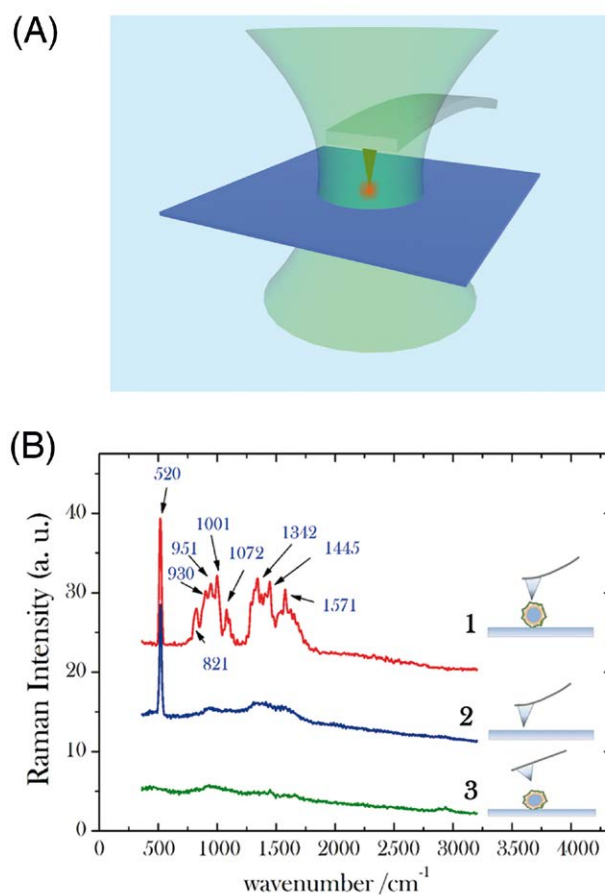Although different kinds of SPM techniques have been

Fig. 7 (A) A scheme of the TERS set-up. (B) a) TERS signal from a point of a biological sample (*B. Subtilis* spore); b) control TERS signal, acquired in a clean part of the glass coverslip; c) signal of the spore, acquired after tip retraction, in the same point of trace a). For a), b) and c) laser power was $P = 50\ \mu W$ and integration time $\tau = 2s$.

realized for TERS systems, an AFM cantilever with metalized tip is the most common choice. Vapor deposition is the simplest method to metalize AFM tips but their yield is usually low due to the random nucleation and growth process of metal NPs around the tip apex.

In order to increase the enhancement factor, the localized surface plasmon wavelength can be finely tuned by changing the material, radius or roughness of the tip apex, to match the wavelength of the excitation laser. Further details about methods to fabricate TERS tips and the geometries to couple the laser with the tip can be found in ref. [13].

As for SERS, we can introduce the Optical Contrast (OC) to quantify the TERS amplification. It is the ratio between the intensity of near-field signal (I_{NF}) and the far-field (I_{FF}) background signal. OC is better defined in terms of the Raman peak intensities measured with the tip in contact (I_{tip-in}) and retracted ($I_{tip-out}$) from the sample with respect to the intensity when the tip is in contact to a reference surface such as clean glass (I_{tip}) as depicted in fig. 7:

(7) $$OC = \frac{I_{NF}}{I_{FF}} = \frac{I_{tip-in} - I_{tip-out} - I_{tip}}{I_{tip-out}}.$$

The enhanced factor EF in a TERS experiment is finally related to the OC by the following equation:

(8) $$EF = \left(\frac{I_{tip-in} - I_{tip-out} - I_{tip}}{I_{tip-out}} \right) \frac{A_{FF}}{A_{NF}},$$

where A_{FF} is the area of the far-field laser probe, while A_{NF} is the effective area of TERS probe, which depends on the geometric diameter of the tip apex.

In fig. 7 we show a typical experimental scheme for TERS system: a linearly polarized laser at 532 nm is focused on the sample through a 60× objective (NA = 0.8, beam waist ~ 370 nm). TERS tips consist of commercial Si-based tips AFM tips; controlled-size Au-NPs of diameter ~14 nm are deposited upon ultrahigh vacuum-conditions.

TERS measurements are not trivial and may be easily affected by artifacts. This is particularly true for soft biological samples. Indeed, to prevent tip-induced artifacts caused by the interaction of the tip with the soft sample surface, AFM analysis is usually performed in tapping mode.

3 SERS and TERS applications to biology

Spontaneous Raman spectroscopy and, more recently, its variants as SERS and TERS, have been widely employed as a label-free chemical characterization tool in life sciences, from macroscopic scale up to micro- and nanoscopic scales. SERS has proved to be an effective platform for bio-sensors, imaging of living-cells, for surface cell sensing, nucleic acid sequencing, etc. Similarly, TERS finds interesting applications for the study of the dynamics and function of pathogens such as bacteria and viruses, to localize specific components on a
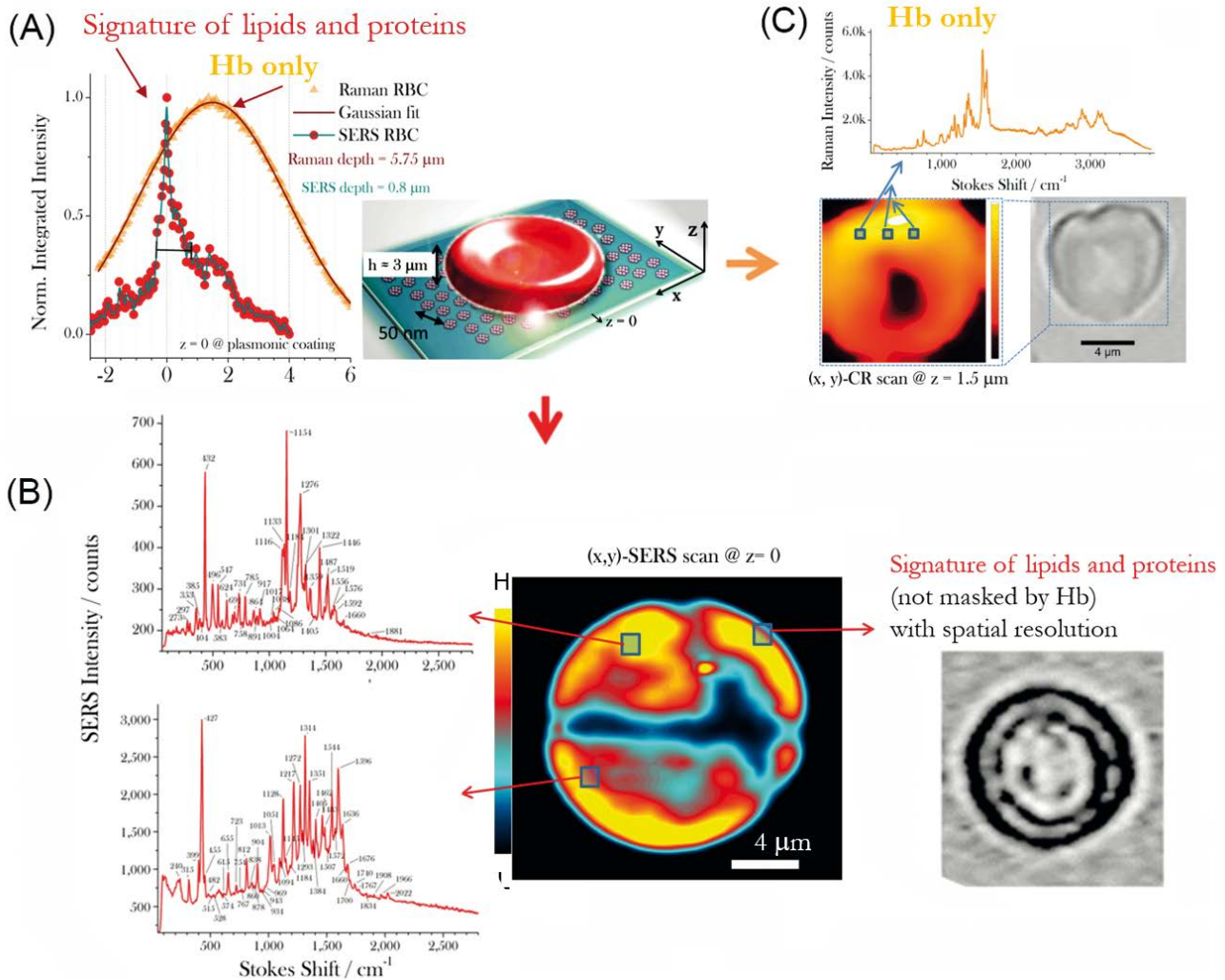
Fig. 8 Axial Raman scanning of RBC to validate membrane detection. (A) Schematic representation of the experiment. The SERS intensity integrated over 1400−1600 cm^{-1}, from the RBC, is localized sharply along the axial coordinate z around the SERS nanostructure position (z = 0) (red points); in contrast, the spontaneous Raman signal gives rise to a broad signal in z – peaked at the RBC equatorial plane located ~1.5 μm above the glass (yellow points) – as a result of the volumetric scattering contribution. (B) Typical SERS spectrum measured at z = 0, which clearly presents spectral markers of membrane lipids and proteins: hyperspectral SERS map S (x, y, z = 0) resulting from scanning the particular cell shown in the optical image on the right. (C) Spontaneous Raman spectrum of the RBC, which shows only typical spectral features of Hb: the variation of the intensity of the Raman map, in this case, represents only the variation of the relative concentration of Hb in the cell volume.

pathogen's membrane (for instance the over-expression of proteins in cancer cells), and to monitor biological processes such as host-pathogen interactions (bacterial adhesion, formation of biofilms, etc.). The wide range of applications of SERS and TERS demonstrates the flexibility of these techniques but also the feasibility for quantitative studies of complex bio-systems.

Here we focus on few specific examples to demonstrate the potentiality of the amplified version of Raman spectroscopy, SERS and TERS.

3.1 SERS imaging of red blood cell membrane

Here we demonstrate how the high spatial reproducibility of block-copolymers−based SERS substrates, discussed above, is able to study the membrane of a single cell, i.e. to separate the membrane response from the bulk inner cell contribution.

We consider red blood cells (RBCs), as cell model, because of the facility to handle them, but also because this cell plays an important role in the human body. Indeed RBC membrane deformability changes in relation to blood diseases and its
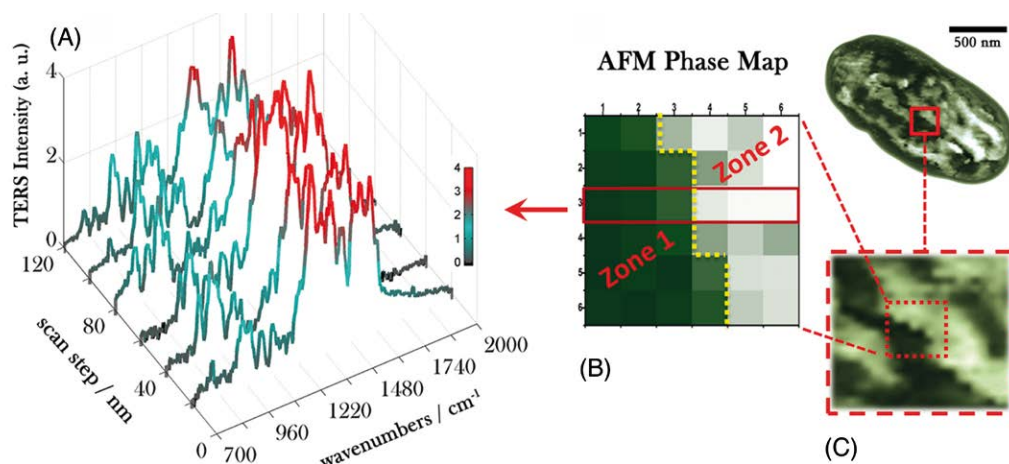
Fig. 9 (A) SEM image of fully dehydrated *B. subtilis*. Spores surface exhibits characteristic ridges resulting from volume contraction due to the core dehydration. (B) AFM phase map of a whole spore acquired in tapping mode. Bright (dark) zones correspond to regions of higher (lower) stiffness. (C) AFM phase map detailed zoom of a selected spore region across a spore ridge: the dashed line defines the border between two zones around the zero-crossing. In particular, zone 2 (exhibiting a higher stiffness) corresponds to a surface ridge. TERS spectra acquired with 20 nm step along the horizontal line are highlighted by the red rectangle in the phase map zoom.

functional glycoproteins determine the cell interaction with the bio-environment [30–33].

SERS detection of RBC membrane is not trivial because of hemoglobin (Hb) presence which is Raman resonant at $\lambda_0 = 532$ nm. The effort is then to identify unambiguously the SERS signal produced by the plasma membrane molecules on the Ag-NPs from the cytosolic Hb.

To this purpose we realized two separate experiments, one with RBC on the Ag-NPs substrate and the other with RBC on a simple coverslip. With the first experiment we expected to detect the SERS spectra of the outer part of the cell while with the second one to detect the spontaneous Raman spectra of the cell bulk. We repeatedly acquired Raman spectra at different heights by scanning along the *z*-axial coordinate, as represented in fig. 8 A. By means of this characterization, we ascertained that the experimental Raman intensity acquired with the SERS substrate was actually localized only at the cell surface since we observed a peak in the SERS intensity (fig. 8 A, red dots) located around the nanostructure height with an effective depth of ~ 800 nm, *i.e.*, well below the measured thickness of the confocal scattering volume ($h_e = 2.6$ μm). SERS spectra were acquired with very low incident power (~3 mW) so that, when penetrating the cell volume, the Raman signature of cytosolic Hb was negligible. In addition the excitation power had to be increased by 3 orders of magnitude prior to inducing any "bulk"-contribution in spontaneous Raman measurements. In this case, the analogous axial response curve measured on RBC on the uncoated coverslip was characterized by a significant broader bell shape given by the intrinsic convolution of the signal resolution with the cell volume (fig. 8 A, yellow dots), peaked around the middle plane of the cell ($z = 1.5$ μm).

In contrast to spontaneous Raman detection, surface SERS spectra ($z = 0$) had a clearly different Raman fingerprint characterized by membrane peaks not observed in previous Raman studies of RBCs (fig. 8 B). As expected, spontaneous Raman spectrum, instead, was mainly ascribable to Hb and was found unvaried at the *z*-coordinate around the membrane (example shown in fig. 8 C).

Finally, we acquired SERS spectra by spatially scanning the cell surface to obtain hyperspectral imaging and to correlate it with optical microscopy. A confocal, lateral spatial resolution of ~200 nm was experimentally determined. The SERS spectra showed spectral features that we assigned mainly to carbohydrates, proteins and phospholipids of the membrane (fig. 8 B). Each membrane position was characterized by a different SERS spectrum, denoting a sensing capability for the local molecular environment explored in the laser scattering area. The representative hyperspectral map shown in fig. 8 B is calculated by integrating the SERS intensity in a wide range of wavenumbers, *i.e.*, 1100–1700 cm^{-1}, to account for the major spectral features, and reveals a strong correlation with the optical image of the same RBC (fig. 8B). It is worth noting that the SERS imaging was possible because of the excellent uniformity of the enhancement factor over a large area of the nanoparticles substrate.

3.2 TERS imaging of spores surface

In this section we show how TERS technique, combined with PCA analysis, is able to analyze, with nanometric resolution, the morphology and the chemistry of a single-cell membrane. In particular, we analyze the coat of *Bacillus subtilis* spore, which is often considered as a model system for spore-forming bacteria and for many bio-technological application, like drug delivery [34], or even as a promising source for new type of energy production [35]. Here we focus on particular surface structures, the so-called spore

Fig. 10 (A) Second and third PC maps of TERS data. The dashed line highlights the boundary between zone 1 and zone 2 in the phase map (the ridge corresponds to zone 2). The scale is everywhere 20 nm. PC-maps reveal a strong spatial correlation with the phase map (color bar: L = low level, H = high level. (B) Related loadings resulting from PCA analysis of the same TERS data map acquired in the square region under consideration.
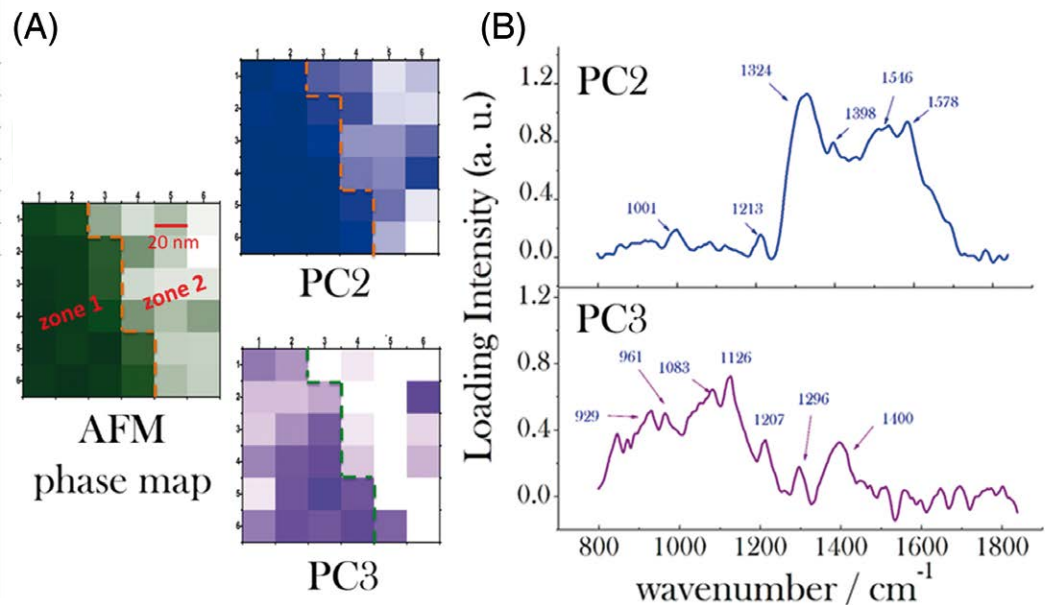
ridges [36], readily distinguishable in the scanning electron micrograph. The function of these structures is still not fully understood; it may be related to the volume changes occurring during spore core dehydration-rehydration cycle.

In order to shed light on this surface chemical heterogeneity, we acquired preliminarily an AFM image of the spore surface. By mapping the phase of the oscillating cantilever in tapping mode, AFM phase imaging provides information about adhesion, friction and viscoelasticity that reflects the different chemical composition of the surface. Figure 9 shows the AFM phase image acquired on an area of 120×120 nm^2 with step of 20 nm across a spore ridge. The TERS spectra acquired along the third row marked in red in the phase map are reported on the left. TERS spectra were acquired by using a laser power of ~ 50 μW and an integration time of 2 s. Interestingly, these exhibit a marked point-to-point variation. Repeated measurements along the same line showed a great reproducibility and thus demonstrating a lateral resolution of ~ 20 nm.

The TERS spectra acquired along the selected surface (fig. 9 C) were processed with principal component analysis, *i.e.* each TERS spectrum was decomposed in principal components (PCs). The result of this analysis is shown in fig. 10 A. The first three PCs were found to account for more than 80% of the total data variance. Since the first component (PC1) revealed only the background contribution, maps were obtained by retaining only PC2 and PC3 components. Interestingly, PC2 and PC3 score maps resemble quite well

the AFM-phase map with higher score corresponding to the ridge zone (see fig. 10 A).

An understanding of the biochemical basis of differentiation between the considered zones 1 and 2, as highlighted by PCA, can be found by inspecting the spectral features in PC2 and PC3 loadings (fig. 10 B). The PC2 loading consists of relatively wide features that are systematically found on the ridge zone. The continuity of the scanning process rules out the possibility of a carbonaceous contamination of the tip; thus, these broad spectral features present in PC2 are more likely ascribable to a denser arrangement of protein amino acids across the ridge, as also evidenced by the intense load on phenyl ring vibration around 1570 cm^{-1}, hydrogen bonded β-turn at 1324 cm^{-1}, and phenylalanine at 1001 cm^{-1} (fig. 10 B, PC2). Analogously to PC2, also the PC3 map presents important overlapping with the phase map zone 2. The sharp spectral features of the third loading (PC3) put into evidence variations in the spectral regions concerning the Raman bands of simple carbohydrates, in particular in the 1100 cm^{-1} region, as well as amino acids related features. However, PC3 also exhibits some unspecific features around 1400 cm^{-1} common to proteins, lipids, and carbohydrates. We speculate that PC3 score map could represent a higher concentration of simple sugars on the ridge surface, responsible of the higher stiffness evidenced in the phase map. In this frame, the ridge might act as a sort of chemical reservoir for bacteria after sporulation of the dormant cells.

References

[1] L. Pavesi and P. M. Fauchet (Editors), "*Biophotonics*" (Springer-Verlag Berlin Heidelberg) 2008.

[2] S. W. Hell and J. Wichmann, "*Breaking the diffraction resolution limit by stimulated emission: Stimulated-emission-depletion fluorescence microscopy*", Optics Lett., 19 (1994) 780.

[3] F. Casadio, C. Daher and L. Bellot-Gurlet, "*Raman Spectroscopy of cultural heritage Materials: Overview of Applications and New Frontiers in Instrumentation, Sampling Modalities, and Data Processing,*" Curr. Chem. (Z), 374 (2016) 62.

[4] Y-S Li and J. S. Church, "*Raman spectroscopy in the analysis of food and pharmaceutical nanomaterials,*" J. Food Drug Anal., 22 (2014) 29.

[5] J. M. Chalmers, H. G. M. Edwards, and M. D. Hargreaves (Editors), "*Infrared & Raman Spectroscopy in Forensic Science*" (Wiley) 2012.

[6] M. Ghomi (Editor), "*Applications of Raman Spectroscopy to Biology: From Basic Studies to Disease Diagnosis*" (IOS Press) 2012.

[7] F. Siebert and P. Hildebrandt, "*Vibrational Spectroscopy in Life Sciences*" (Wiley-VCH) 2008.

[8] A. C. De Luca, G. Rusciano, R. Ciancia, V. Martinelli, G. Pesce, B. Rotoli and A. Sasso, "*Spectroscopical and Mechanical Characterization of Normal and Thalassemic Red Blood Cells by Raman Tweezers*", Opt. Express, 16 (2008) 7943.

[9] A. Zumbusch, G.R. Holtom, X.S. Xie, "*Three-Dimensional Vibrational Imaging by Coherent Anti-Stokes Raman Scattering*", Phys. Rev. Lett., 82 (1999) 4142.

[10] Fa-Ke Lu, D. Calligaris, O. Olubiyi, I. Norton, W. Yang, S. Santagata, X.S. Xie, A.J. Golby, N.Y.R. Agar, "*Label-Free Neurosurgical Pathology with Stimulated Raman Imaging*", Cancer Res., 76 (2016) 3451.

[11] E. C. Le Ru and P. G. Etchegoin, "*Principles of Surface-Enhanced Raman Spectroscopy: And Related Plasmonic Effects*" (Elsevier) 2009.

[12] K. Kneipp, Y. Wang, H. Kneipp, L. T. Perelman, I. Itzkan, R. R. Dasari, and M. S. Feld "*Single Molecule Detection Using Surface-Enhanced Raman Scattering (SERS)*", Phys. Rev. Lett., 78 (1997)1670.

[13] S. Kawata V. and M. Shalaev (Editors)., "*Tip Enhancement*", in "*Advanced nano-optics and nano-photonics*" (Elsevier) 2007.

[14] B. S.Yeo, J. Stadler, T. Schmid, R. Zenobi, W.H. Zhang, "*Tip-Enhanced RamanSpectroscopy : Its Status, Challenges and Future Directions*" Chem. Phys. Lett., vol. 472 (2009) 1.

[15] B. S.Yeo, S. Maedler, T. Schmid, W.H. Zhang, R. Zenobi, "*Tip-Enhanced Raman Spectroscopy Can See More: The Case of Cytochromec*", J. Phys. Chem. C, 112, (2008) 4867.

[16] M. Fleischmann, P. J. Hendra and A. J. McQuillan, "*Raman spectra of pyridine adsorbed at a silver electrode*", Chem. Phys. Lett., 26 (1974)163.

[17] D. L. Jeanmaire and R.P.Van Duyne, "*Surface Raman spectro-electrochemistry, part 1: heterocyclic, aromatic, and aliphatic amines adsorbed on the anodized silver electrode,*" J. Electroanal. Chem., 84 (1977) 120.

[18] M. G. Albrecht and J. A. Creighton, "*Anomalously intense Raman spectra of pyridine at a silver electrode*", J. Am. Chem. Soc., 99 (1977) 5215.

[19] P. Roelli *et al.,* "*Molecular cavity optomechanics as a theory of plasmon-enhanced Raman scattering*", Nat. Nanotechnol., 11 (2016) 164.

[20] M. Moskovits, "*Surface-enhanced spectroscopy*", Rev. Mod. Phys., 57 (1985) 783.

[21] G. Zito, G. Rusciano and A. Sasso, "*Enhancement factor statistics of surface enhanced Raman scattering in multiscale heterostructures of nanoparticles.*", J. Chem. Phys., 145 (2016) 054708.

[22] P. C. Lee and D. Meisel, "*Adsorption and surface-enhanced Raman of dyes on silver and gold sols*", J. Phys. Chem., 86 (1982) 3391.

[23] G. Zito, G, Rusciano, G. Pesce, A. Dochshanov, A. Sasso, "*Surface-enhanced Raman imaging of cell membrane by a highly homogeneous and isotropic silver nanostructure,*" Nanoscale, 7 (2015) 8593.

[24] W. J. Cho, Y. Kim and J. K. Kim, "*Ultrahigh-density array of silver nanoclusters for SERS substrate with high sensitivity and excellent reproducibility,*" ACS Nano, 6 (2012) 249.

[25] S. Torquato and F. Stillinger, "*Local density fluctuations, hyperuniformity, and order metrics*", Phys. Rev. E, 68 (2003) 041113, .

[26] C. De Rosa, F. Auriemma, C. Diletto, R. Di Girolamo, A. Malafronte, P. Morvillo, G. Zito, G. Rusciano, G. Pesce, A. Sasso, "*Toward hyperuniform disordered plasmonic nanostructures for reproducible surface-enhanced Raman spectroscopy*", Phys. Chem. Chem. Phys., 17 (2015) 8061.

[27] G. Zito *et al.*, "*Nanoscale engineering of two-dimensional disordered hyperuniform block-copolymer assemblies*", Phys. Rev. E, 92.5 (2015) 050601.

[28] G. Zito *et al.* "*Nanometal Skin of Plasmonic Heterostructures for Highly Efficient Near-Field Scattering Probes*", Sci. Rep., 6 (2016) 31113.

[29] L. Novotny and B. Hecht "*Principles of Nano-Optics*", Second Edition (Cambridge University Press) 2012.

[30] J. Wessel "*Surface-enhanced optical microscopy*", J. Opt. Soc. Am. B, Opt. Phys., 2 (1985) 1538.

[31] R. M. Stockle, Y. D. Suh, V. Deckert, R. Zenobi, "*Nanoscale chemical analysis by tip-enhanced Raman spectroscopy*", Chem. Phys. Lett., 318 (2000) 131.

[32] Y. Park *et al.*, Proc. Natl. Acad. Sci. U.S.A., 105 (2008) 13730.

[33] A. C. De Luca *et al.*, Opt. Express, 16 (2008) 7943.

[34] E. Ricca and S.M.Cutting, "*Emerging Applications of Bacterial Spores in nanobiotechnology*", J. Nanobiotech., 1 (2003) 1.

[35] X. Chen, L. Mahadevan, A. Driks, O. Sahin, "*Bacillus Spores as Building Blocks for Stimuli Responsive Materials and Nanogenerators*", Nat. Nanotechnol., 9 (2014) 137.

[36] G. Rusciano, G. Zito, R. Isticato, T. Sirec, E. Ricca, E. Bailo, A. Sasso, "*Nanoscale chemical imaging of bacillus subtilis spores by combining tip-enhanced Raman scattering and advanced statistical tools*", ACS Nano, 8 (2014) 12300.

Antonio Sasso

Antonio Sasso was born in Naples (Italy) in 1956. He received his academic education at the University of Naples "Federico II", where he got his degree in physics in 1980. From 1989 to 1991 he was Humboldt fellow in the group of Prof. W. Demtroeder at the University of Kaiserslautern. His general field of research is in the area of laser-matter interaction, with applications to high resolution and high-sensitivity laser spectroscopy. More recently his activity is focused on optical manipulation of microparticles and cells, and on the development of advanced Raman techniques (Surface Enhanced Raman Scattering and Tip-Enhanced Raman Spectroscopy) for the study of soft matter and bio-systems. Currently he is Full Professor at the University of Naples and group leader of the Laser Spectroscopy and Optical Manipulation Laboratory.